Shaped pupil coronagraphy for WFIRST: high-contrast broadband testbed demonstration

Eric Cady[a]*, Kunjithapatham Balasubramanian[a], Jessica Gersh-Range[b], Jeremy Kasdin[b], Brian Kern[a], Raymond Lam[a], Camilo Mejia Prada[a], Dwight Moody[a], Keith Patterson[a], Ilya Poberezhskiy[a], A J Eldorado Riggs[a], Byoung-Joon Seo[a], Fang Shi[a], Hong Tang[a], John Trauger[a], Hanying Zhou[a], Neil Zimmerman[c]

[a] Jet Propulsion Laboratory, California Institute of Technology, Pasadena, CA, 91109 USA
[b] Department of Mechanical and Aerospace Engineering, Princeton University, Princeton, NJ, 08540 USA
[c] NASA Goddard Space Flight Center, Exoplanets and Stellar Astrophysics Laboratory, 8800 Greenbelt Rd, Greenbelt, MD 20771

ABSTRACT

The Shaped Pupil Coronagraph (SPC) is one of the two operating modes of the WFIRST coronagraph instrument. The SPC provides starlight suppression in a pair of wedge-shaped regions over an 18% bandpass, and is well suited for spectroscopy of known exoplanets. To demonstrate this starlight suppression in the presence of expected on-orbit input wavefront disturbances, we have recently built a dynamic testbed at JPL analogous to the WFIRST flight instrument architecture, with both Hybrid Lyot Coronagraph (HLC) and SPC architectures and a Low Order Wavefront Sensing and Control (LOWFS/C) subsystem to apply, sense, and correct dynamic wavefront disturbances. We present our best up-to-date results of the static SPC mode demonstration from the testbed, along with model comparisons and performance under realistic dynamical conditions. HLC results will be reported separately.

1. INTRODUCTION

Direct detection of reflected light from exoplanets is a challenging observation to perform today. The extreme ratio in flux between host star and exoplanet—$10^{-8} - 10^{-9}$ for a Jupiter-twin and approximately 10^{-8} for an Earth-twin in the visible[1]—requires very high levels of starlight suppression at the location of the planet in the focal plane, and the distance to stars in the local neighborhood (and the diameters of available telescopes) mean that most accessible planets will be within a handful of λ/D of their host star, even in the visible.

One method for doing this suppression is to use a coronagraph, a name for a general class[2] of high-contrast imaging instruments which use a series of masks and/or remapping optics to filter on-axis starlight while allowing planet light through at a few λ/D. The Wide-Field InfraRed Survey Telescope (WFIRST)[3] will have a coronagraphic instrument (CGI) to do exactly this for stars in our local neighborhood.

One particular challenge of this telescope is the WFIRST aperture, which is on-axis with a large secondary obscuration and relatively wide struts. Prior designs for dedicated space-based coronagraphs (e.g. TPF-C[4], ACCESS[5], EXCEDE[6], PECO[7], EXO-C[8]) generally expected an off-axis configuration with an unobstructed aperture, and prior to the start of WFIRST CGI technology development, an intensive community discussion on the state-of-the-coronagraphic-art downselected to three possible coronagraph configurations usable with the aperture available. (Since that time, the limitations imposed by the telescope helped to re-ignite interest in designs for coronagraphs for obscured apertures[9,10,11], suitable for use in ground-based 30m-class telescopes and future space missions such as LUVOIR[12].)

This instrument will feature two coronagraph types suitable for use with the WFIRST aperture. The first is the shaped pupil coronagraph (SPC)[13], which relies on an optimized pupil mask which overlaps the aperture and reshapes the PSF to match a hard-edged focal-plane mask and Lyot stop downstream, which remove the starlight. The second is the hybrid Lyot coronagraph (HLC)[14], which combines large shapes on two deformable mirrors (DMs) with a complex-valued focal-plane mask and a Lyot and field stop to remove the starlight. These are optimized for use with different science cases, but will be swappable by rotating wheels to move masks in and out of the optical path.

For both the SPC and HLC architectures, new technology was needed to manufacture usable masks. For SPC, previous designs[15,16] were transmissive, and could be made as a series of etched holes in silicon-on-oxide (SOI) wafers. SPC designs suitable for the WFIRST aperture had disconnected regions and needed to be placed in a reflective configuration with a highly-absorbing material defining the mask shape, something which had not been tested previously. Similarly, while previous tests with HLC masks used a linear occulter[17] and a nominally-flat DM, HLC designs suitable for WFIRST CGI required a circular mask with metal and dielectric layers and the careful setting of both DMs against each other and the upstream pupil, again a new technology.

The fact that coronagraphs for WFIRST required previously-untested techniques to meet performance in turn led to a extensive laboratory verification program, to show that the two architectures could be built and work successfully as intended. As part of this, a series of nine technology development milestones were established, reviewed by an independent Technical Assessment Committee (TAC), to verify the underlying technologies work together as expected. The final of these, CGI Technology Milestone #9 (MS9), was required that the system "demonstrates 10^{-8} raw contrast with 10% broadband light centered at 550 nm in a simulated dynamic environment."

In this paper, we report the successful demonstration of MS9 with the SPC coronagraphic architecture. Section 2 will provide an overview of the hardware and coronagraphic optics used, Section 3 will discuss the performance results, and Section 4 will cover the next steps for technology development. The demonstration for HLC, likewise successful, will be reported in [18], while modeling results for SPC Milestone 9 will be in [19] and the demonstration of SPC nulling with an IFS can be found in [20].

2. EXPERIMENTAL SETUP

2.1 Testbed

In order to test the combined coronagraphic system, a new testbed, the Modelable Coronagraph Bench (MCB), was built and installed in February of 2016. This testbed was intended to incorporate the functionality and lessons learned from previous CGI milestones run on individual testbeds[21,22,23] into a flight-like combined system which permits them to all be used in concert. The original layout of the bench is shown in Fig. 1.

The testbed is located in vacuum chamber #1 in the High Contrast Imaging Testbed (HCIT) at JPL, referred to as HCIT-1. HCIT-1 is a 6-foot diameter chamber with a 7.5-foot cylindrical section, and can accommodate tables up to 8 feet in length when accounting for the outward bulge of the endcap doors. Power cables, data cables, water lines, and optical fibers are fed through ports in the sidewalls. Two ports are occupied by camera umbilicals to connect bench-mounted camera enclosures to the lab air, which permit us to use Andor Neo sCMOS cameras as our science detectors in the chamber despite their lack of vacuum compatibility.

The bench itself is a 6.5ft by 4ft invar optical table placed on 3 Minus-K 500CM-1 isolator legs to passively isolate the bench from vibrations. These legs have a manual adjustment range that allows them to retuned to account for changes in weight distribution on the table following hardware modifications.

A telescope simulator on a subbench is kinematically mounted to the northwest corner of the bench, and simulates the front end of the telescope. This includes a jitter mirror (JM) to inject tip/tilt errors into the coronagraph in a controlled manner and a simulator for the optical telescope assembly (OTA) which defines the upstream pupil and permits focus to be injected as well. A higher-fidelity representation of the OTA, which includes mirrors with the same f-numbers as the fast f/1.2 WFIRST primary and secondary, is scheduled to be inserted later this year, and will permit astigmatism, coma, and spherical to be injected in addition to focus. The OTA subbench and bench have a collimated interface, both for ease of alignment and to make the flight baseline.
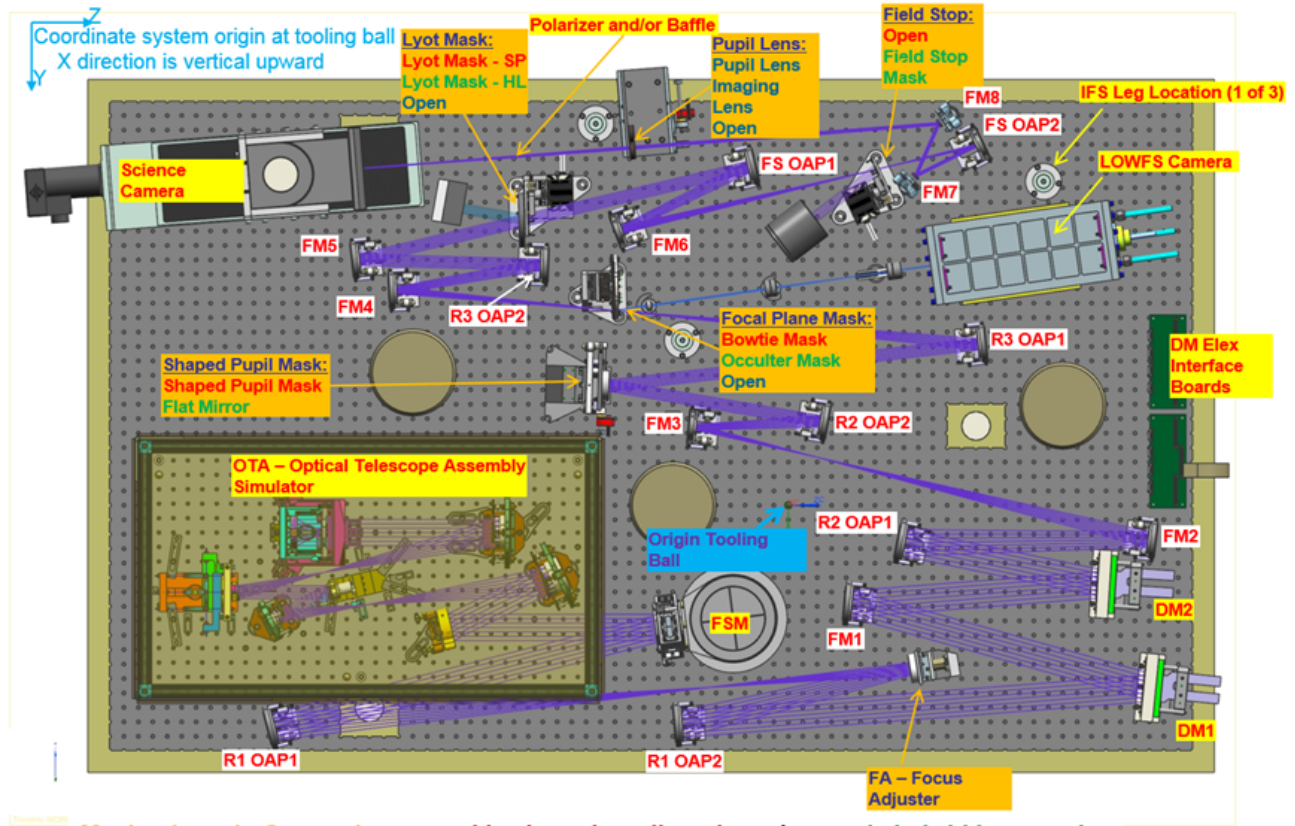
Figure 1. Layout of the MCB at time of installation. Since installation, the telescope simulator on the front end has been replaced, and a wheel with polarizers and bandpass filters was introduced upstreams of the pupil lens. A diffuser can also be slid into place after FM2 to permit the focal plane mask to be imaged more easily.

Within HCIT-1, the bench and OTA subbench are on independent PI thermal control loops which stabilize the mean bench temperature to 30mK P-V under normal conditions. The chamber itself is controlled to a setpoint above laboratory ambient by a PID loop implemented with heater tape under an insulation layer, and can be stabilized to 50mK P-V. All optical mounts were machined from invar with optics bonds within flexure mounts, to minimize the effect of residual thermal fluctuations on the system. The primary heat sources on the table are the two cameras (science and LOWFS), and the DM electronics, and all are cooled by a pair of external water-cooling loops.

In order to change coronagraphs, change bands, and perform pupil imaging, the testbed actuates masks, filters and lenses at 6 planes: 2 pupil planes and 2 focal planes for masks, and 2 intermediate planes in collimated space for changing filters and polarizers and switching to a pupil imaging mode. These use a mix of linear stages and wheels, with the wheels preferred when several masks need to be swapped at a plane. The flight CGI will use wheels for mask switching and some short-distance translation stages for touch-up alignment, but the design an configuration of these mechanisms is not finalized, and it did not make sense to attempt to fully replicate that aspect of the flight configuration.

2.2 Low- and High-Order Wavefront Sensing and Control

Unfortunately for us, carefully aligning an optical testbed and inserting a coronagraph will not get you 10^{-8} contrast on its own, not without satisfying extreme tolerances on manufacturing and stability. A simpler and more effective way to reach those contrasts is by wrapping one or more control loops around the optical system, to active correct by unwanted light or instabilities.

For wavefront estimation and correction, the MCB bench uses a series of sensors and actuators that can correct different modes on different timescales. As with prior high-contrast demonstrations in HCIT, high-order wavefront estimation is done with pairwise probing[24], which uses structured DM modulation to interfere starlight with speckles in the focal-plane region of interest (the "dark hole"). The residual electric field may then be extracted from a series of images of these DM probes. This method is sensitive only to static (or quasi-static) errors, and usually one confined to the mid spatial frequencies.

Correction of these speckles is done with electric field conjugation (EFC)[25]. This algorithm attempts to minimize the residual speckle intensity in a least-squares sense by inverting a Jacobian, a matrix of electric-field sensitivity to individual DM actuator pokes. This inversion is currently regularized with a single parameter (Tikhonov regularization), which can be changed between iterations. In the process of MS9 completion, we discovered that adjusting this parameter per iteration can improve the overall contrast achieved, and have used "control strategies", sequences of regularization parameter settings, to produce our best contrast results. See [26] for a more in-depth description of the mathematics behind the scheduling in control strategies.

The primary sensor for low-order dynamic errors is the Low-Order Wavefront Sensor (LOWFS), here a Zernike wavefront sensor[27,28,29] combining the rejected light from the focal-plane mask with a phase-shifting spot to turn phase errors into amplitude errors visible with a camera. This sensor can measure tip-tilt errors at 500Hz and correct them with a feedback loop hooked into a pupil-plane fast steering mirror (FSM)[30] in the front end of the coronagraph. Strong errors at specific known frequencies can also be corrected by a feedforward loop with an least mean square (LMS) estimator[30]. While the feedforward loop was originally implemented to correct injected tones which are representative of telescope resonances induced by the reaction wheel assembly (RWA), we also have found the scheme useful in practice in the testbed to correct 60Hz tones and their harmonics, which we have found to be strong contributors to residual uncommanded jitter on MCB.

In addition to tip/tilt, the LOWFS sensor measures and tracks changes in low-order Zernike modes: focus, astigmatism, coma, trefoil, and spherical aberration. (The measurement is inherently differential, comparing the current state to a reference; it is not an absolute sensor.) We build the reconstructor for these modes empirically, chopping Zernike-mode phases embedded in the DM to get signal and reference. (See myfigfig:empmode.) The LOWFS can, in principle, track other modes as well. One mode we found essential to track for SPC operation was the shear of the pupil on the LOWFS camera, as the differential signal induced by shearing the measured signal against the reference signal printed spuriously into all other tracked low-order modes if not accounted for. For further discussion of the MCB LOWFS sensor and its implementation, see [31].

For correction of low-order Zernikes, we are using one of our deformable mirrors. (For flight, focus will be corrected by a dedicated focus adjuster, but this is not fully implemented in the MCB and was not used for MS9 testing.) Given the per-actuator response in height to voltage commands, we can send the DM to approximate the shape of any of these low-order modes; our primary limitation is our knowledge of the DM response, rather than e.g. the high-frequency errors created by the actuator influence functions.

A dedicated server was written to drive LOWFS measurements to tracking reference points by combining low-order DM settings with commanded DM settings for probing and dark-hole digging prior to sending the commands to the DM electronics. The control loop is implemented as a discrete integrator loop on the tracking error term, with saturation. Tracking offsets are also recomputed every time a new DM setting is applied, so that the loop does not attempt to correct intentional insertion of low-order terms, or the low-order projections of unrelated settings. This permits either or both of the low-order correction and the high-order correction (or other operations) to be run simultaneously, without either needing to know about the other.

2.3 Masks

Mask configuration for the SPC half of MS9 is an advancement on the two-mask design from [21]: in addition to a shaped pupil and a hard-edged focal plane mask, it adds a Lyot stop at a subsequent downstream pupil. The masks, and the fields at each plane, can be seen in Fig. 3. Adding a Lyot stop enables smaller inner working angles in designs[32], at the cost of increasing alignment tolerances on the focal plane masks.

The shaped pupils are reflective masks, made by using black silicon processing[33] on a 4mm aluminum-coated silicon wafer to create highly-absorbing regions which define the optimized pupil shape. The focal-plane masks
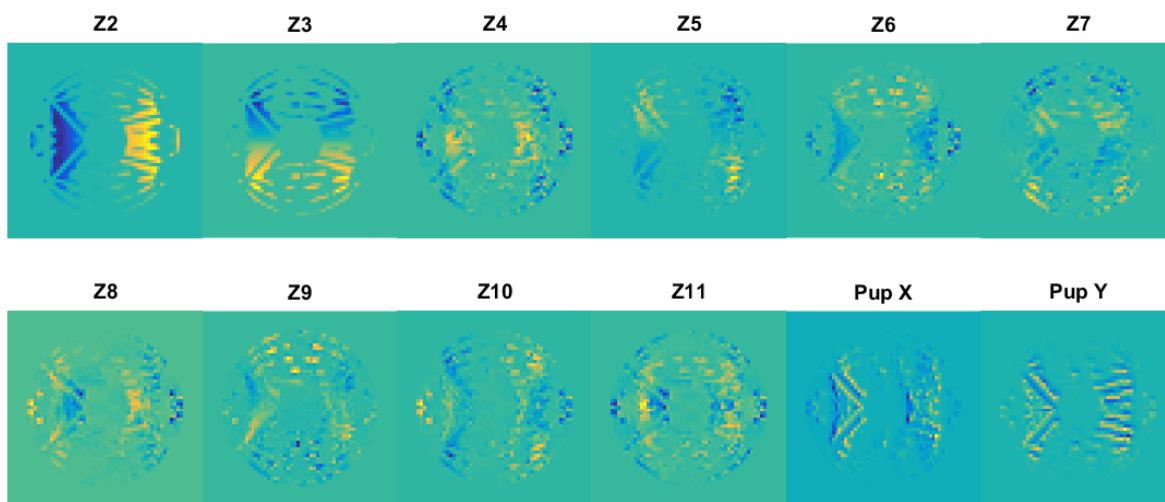
Figure 2. Empirical mode shapes used for wavefront reconstruction in LOWFS. Z2 and Z3 are measured from tip/tilt mirror motions, Z4-Z11 are measured by placing Zernikes on one of the DMs, and pupil X and Y shear are built by shearing reference images.
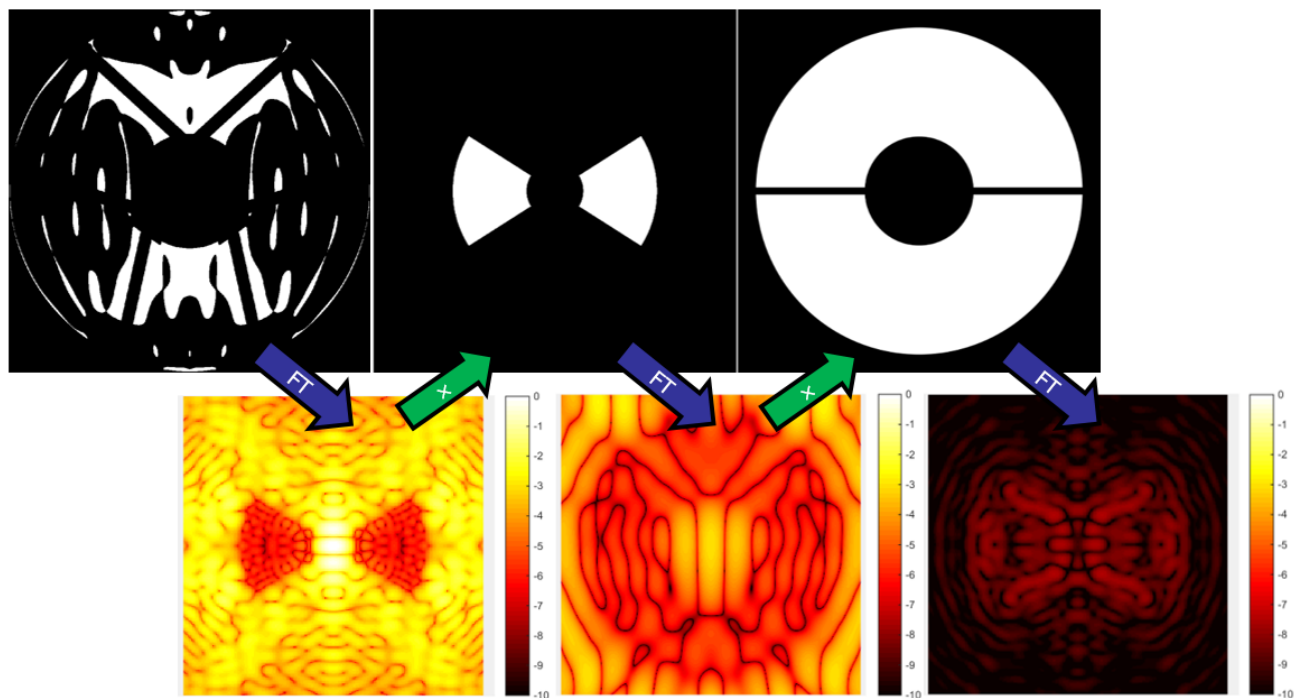

Figure 3. Masks and intensity distributions in an SPLC. A Fourier transform (FT) takes each mask to next intensity distribution, where it's then multiplied by the next mask. *Top row.* The three masks used in the shaped pupil; all are binary masks. Left is the shaped pupil, center is the focal-plane mask ("bowtie") and right is the Lyot stop. *Bottom row.* Intensity distribution before the bowtie mask, before the Lyot stop, and at the camera.
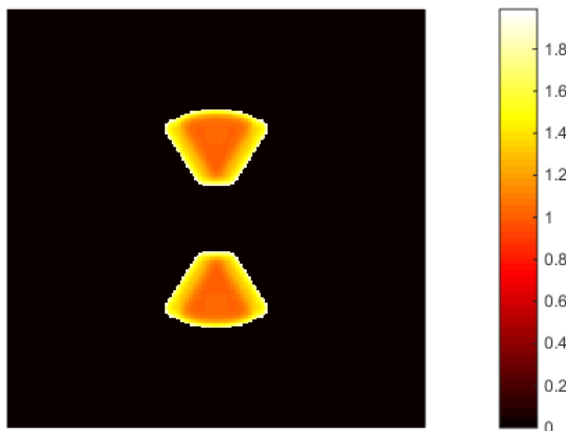
Figure 4. Spatial distribution of the per-pixel correction factor which multiplies the normalized intensity to correct for the throughput of a planet off-axis. The function is masked beyond points where we would get < 50% plane throughput.

and Lyot stops are both made by creating holes in silicon-on-oxide wafers by deep reactive ion etching. For more on the manufacturing of the masks, see [34].

3. PERFORMANCE RESULTS

Prior to showing performance results, we need to discuss the metrics used.

"Normalized intensity" or "NI" at a point in the dark hole is the raw PSF, normalized so that the PSF peak is 1. This is the data produced by camera images to within a constant normalization parameter, and so is convenient for relating to actual data. Weighting across the image plane is uniform.

"Raw contrast", often abbreviated to "contrast", is the normalized intensity multiplied by a field-angle-dependent scaling factor which accounts for the losses in planet flux through the coronagraph as a function of angle. One of these distributions is shown in Fig. 4. Contrast is always greater than or equal to normalized intensity at any point in the focal plane, though in practice we remove points where the planet throughput is less than 50% as not usable. The changing value of throughput across the image plane means than averages of contrast will tend to place higher weights on points near edges of focal-plane masks, particularly for SPC.

As a scientific metric, contrast is more applicable, and was required for all CGI Milestones, but for testbed data analysis normalized intensity is often desirable as the results are not skewed by the throughput weighting.

3.1 Static performance

Static performance for a coronagraph is a limiting case: how deep of a dark hole can be achieved in practice under conditions approaching ideal? The performance will be bounded by several factors: coronagraph design, control scheme design, testbed/instrument stability, testbed/instrument quality, and model quality. Coronagraph design sets the fundamental floor; the remaining factors must be kept under control by systems engineering and modeling in conjunction with an error budget.

Prior to the installation of the MCB, the shaped pupil coronagraph was tested on a dedicated static testbed. CGI Technology Milestone #5 (MS5) was a static demonstration milestone of both SPC and HLC contrast across a 10% band; it was intended to show that both coronagraphic architectures worked with no significant showstoppers. These results were presented to, and accepted by, the CGI TAC in September of 2015. Fig. 5 shows coronagraph performance at that stage of CGI testing, with three separate runs producing $< 8.8 \times 10^{-9}$ contrast averaged across the dark hole.
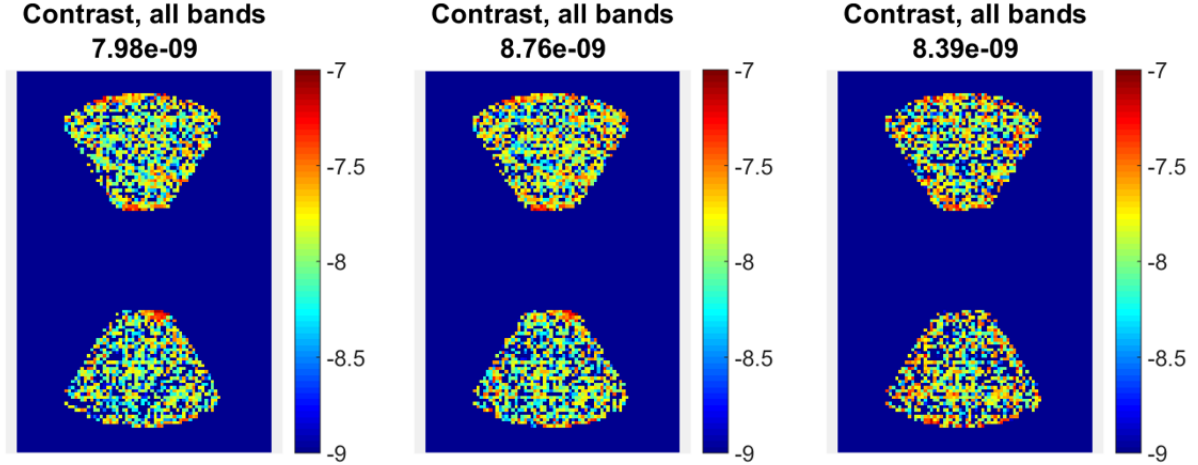
Figure 5. Image-plane contrast distributions in the final iteration of each SPC MS5 run in September 2015.

In the absence of dynamically-injected errors, the LOWFS control system may be used mitigate testbed stability issues such as vibration-induced jitter and slow thermal drifts. Given this, we expect to be able to push to deeper static contrasts with MCB if the tip-tilt and low-order control systems are engaged, and in practice we find that to be the case. Fig. 6 shows the best static performance achieved with MCB: 4.08×10^{-9} averaged across an 11% band.

While these tests were performed over 10% bands, consistent with bandpasses for the CGI imager, the IFS will operate over one of 3 18% bandpasses. Recent static tests using the IFS directly as the source of data for wavefront sensing and control demonstrated a contrast of 1.09×10^{-8} averaged over an 18% band, shown in Fig. 7. See [20] for more details.

3.2 Dynamic performance

Given successful static performance, the next challenge—and subject of MS9—was to test the coronagraph under realistic dynamic errors, particularly random pointing tip-tilt jitter and slow simulated thermal variations.

Error injection for MS9 was done in parts, with two optics. Jitter was injected at a tip-tilt mirror in a conjugate pupil. Either of two terms could be added independently:

1. An offset randomly chosen from the WFIRST attitude control system (ACS) bandwidth to represent the pointing residuals of the WFIRST telescope. For MS9, we used 14 mas rms per axis, as this was the worst-case ACS residual expected from the telescope at the time.

2. One or more tones to represent vibration induced by the reaction wheel assembly. For this test, the best approximation to RWA tones for operation at 600rpm were used, with the primary harmonic at 10Hz and 72 tones in total.

For wavefront drift above tip-tilt induced by thermal variations, focus modulation was used as a surrogate, as integrated modeling showed focus variation would be the primary contributor to low-order RMS wavefront variation for changes in thermal environment[23]. Focus was injected by actuating the stage holding the input fiber along the beam axis; 30μm of z-motion induced 1 nm rms of focus. While expected levels of focus from integrated modeling results were on the order of 0.5nm rms focus peak-to-valley over 24 hours[23], we ended up inserting 4× this amount ($\pm$1nm rms focus), as if lower amounts (e.g. 2×) were used, the perturbations were barely discernable. The input profile was sinusoidal with a 12.5 minute period. Correction of injected low-order errors was done with the methods described in Section 2.2.

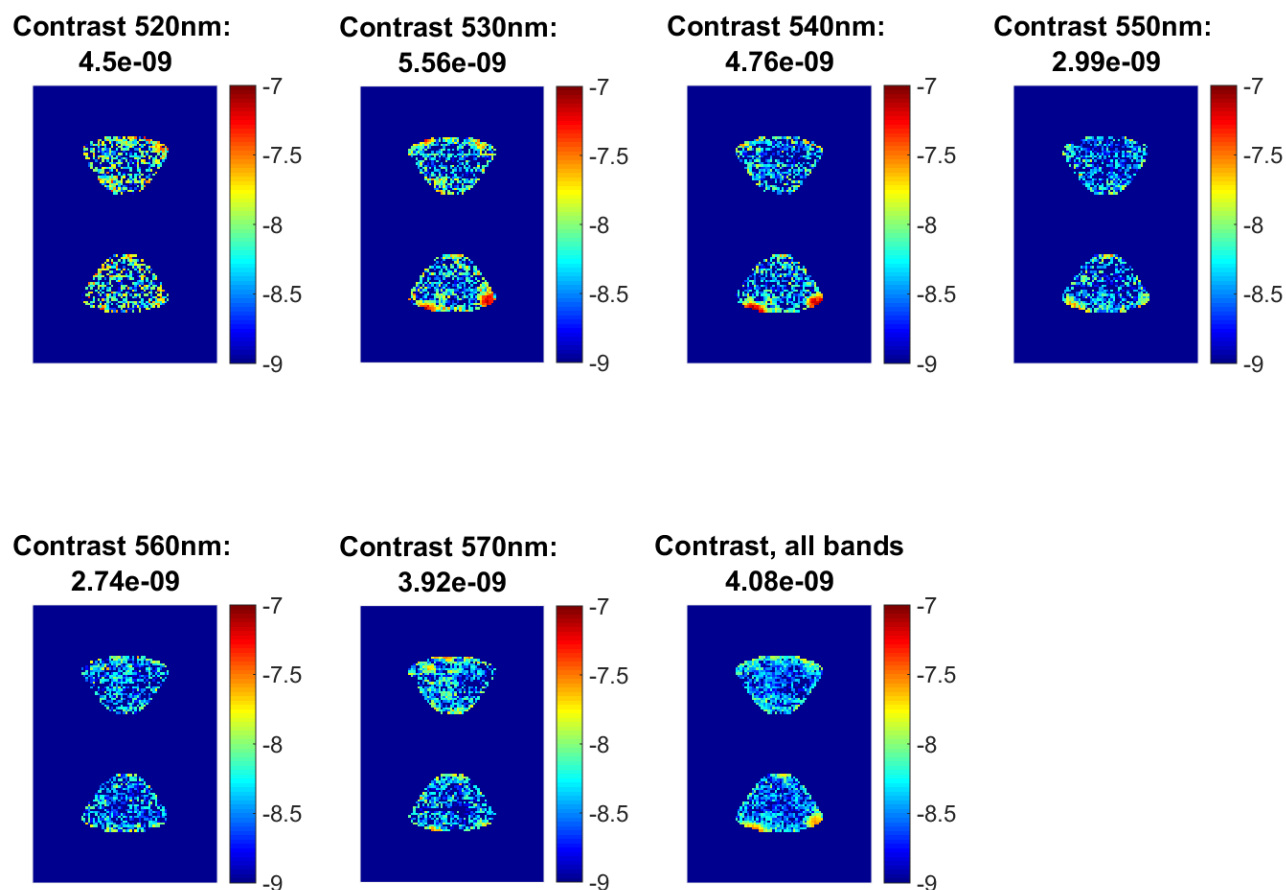The test sequence shown in Fig. 8 has six segments:

Figure 6. Image-plane contrast distributions for SPC with LOWFS correction of tip, tilt, and focus over 60nm band, June 2017. Source band was kept fixed at 20% for LOWFS stability, and each 10nm band was introduced by rotating in a fixed filter.
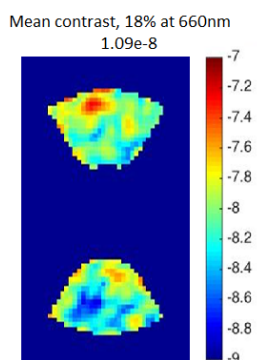

Figure 7. Image-plane contrast distribution for SPC correction across 18% band with the PISCES IFS, May 2017. This testbed has a separate imaging camera, but wavefront sensing and control was done with IFS data only.
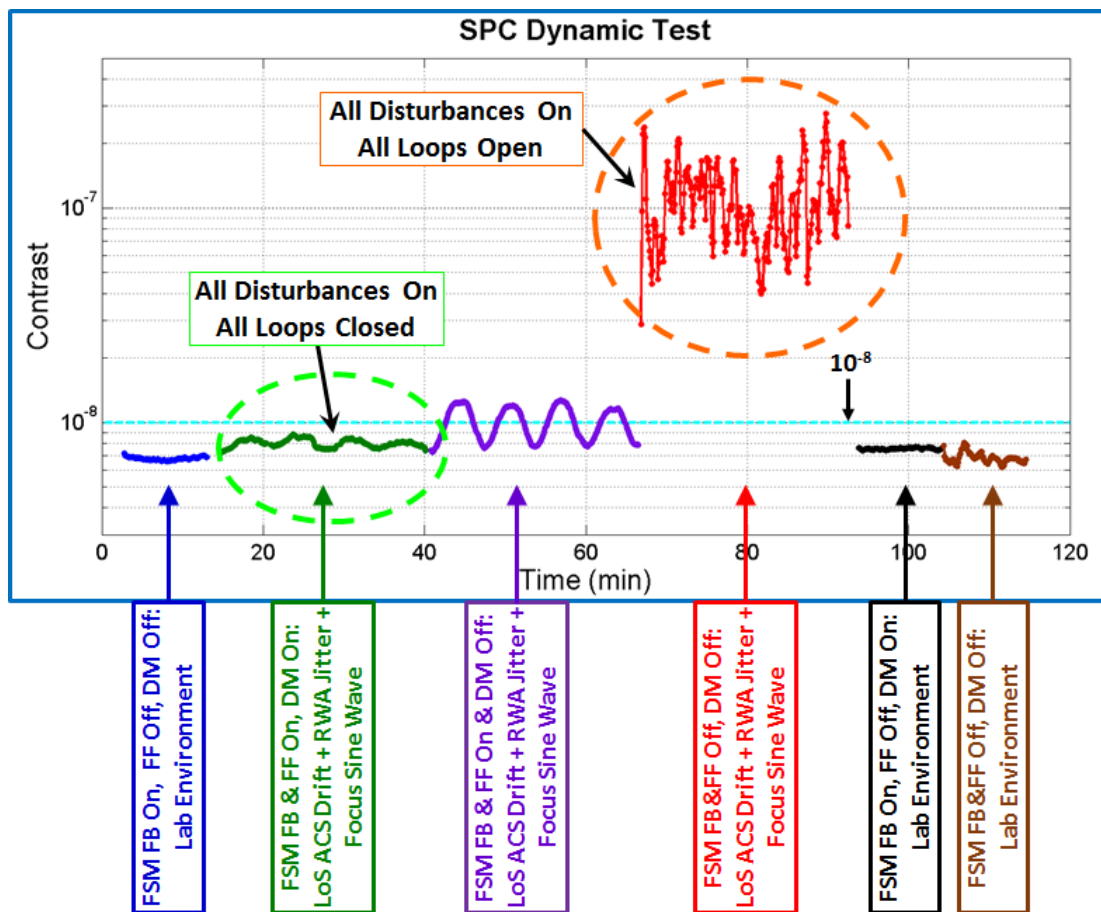
Figure 8. Contrast vs. time for the MS9 test sequence. Injected perturbations can either be ACS + RWA + focus or standard lab environment; corrections, if used, may be a combination of feedback control of tip-tilt (FB), feedforward control of tip-tilt (FF), and DM-based focus correction. The green segment has all injections and all corrections; the red segment has all injections and no corrections.

Mean 10% contrast: 8.94e-9
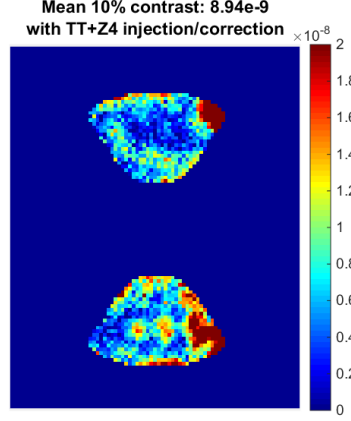**with TT+Z4 injection/correction**

Figure 9. Contrast after nulling SPC with all perturbations and loops enabled.

1. Segment 1: Feedback loop closed, lab environment (i.e. no injections). Intended to lock up star location to prevent any drift before starting injections.

2. Segment 2: All disturbances on, all loops closed (FB/FF/focus). From a floor of 7.8×10^{-9}, ± 1nm of focus offset with correction produced 5.8×10^{-10} contrast increase, which we attribute to the residuals from focus correction. This residual is a mixture of focus uncorrected by the control loop and miscalibration of DM response.

3. Segment 3: Here the DM loop was turned off and monitored for two cycles, each of which make two peaks, positive and negative. From a floor of 7.8×10^{-9}, ± 1nm of focus offset produced 4.6×10^{-9} contrast increase, slightly lower than the expected sensitivity to source motion (see Section 3.3), but $8\times$ larger than the residuals in segment 2.

4. Segment 4: Here the feedback and feedforward loops were also turned off; in the absence of any correction, dynamic errors will limit SPC raw contrast to a mean of 1.1×10^{-7}.

5. Segment 5: All perturbations were turned off, and the feedback and DM loops were turned on to remove testbed jitter and thermal drift. Contrast was stable to 6.6×10^{-11} rms over the 10 minutes of this sequence, which is likely the stability limit of the testbed as currently implemented with SPC.

6. Segment 6: All loops were turned off.

We had originally ran this test sequence with 1nm P-V focus injection, but the residuals even with the DM loop off were quite small (still less than $< 10^{-8}$ contrast), so we doubled the injection amplitude for the data set in Fig. 8.

Given this, we can confidently say that the SPC and the LOWFS can be used together to maintain high contrast even in the presence of the flight-like dynamic errors. (The HLC testing was also successful; see [18] for details.) The CGI TAC agreed, and passed MS9 in January of 2017.

A few months after this testing sequence, we ran a separate test to verify that SPC could null successfully under the presence of injected errors. For this we used the same components to inject and correct errors, but instead of holding a dark hole at $< 10^{-8}$, we started with a DM setting producing a mediocre dark hole (3.94×10^{-7}) and nulled as shown in Fig. 9. While the correction does work successfully, there is room for improvement, as the final contrast—8.94×10^{-9}—is not yet at the levels seen in static testing.
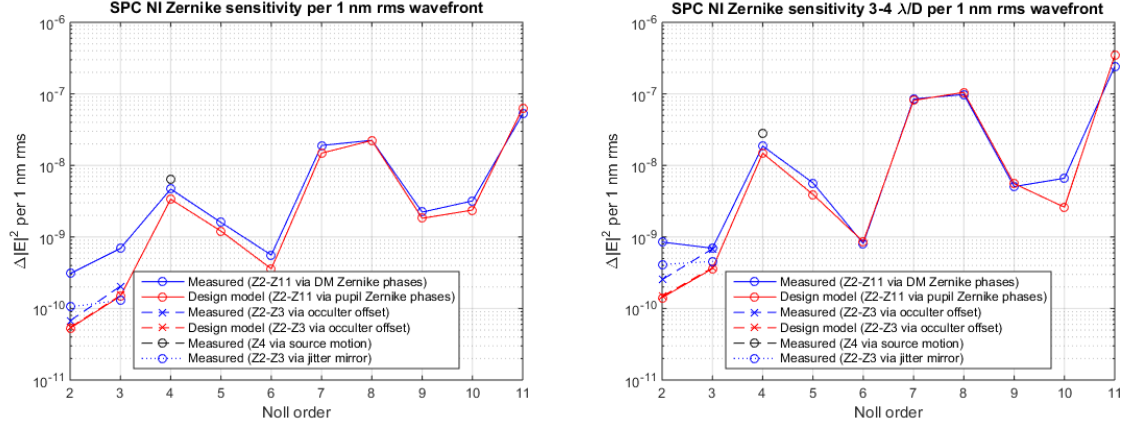
Figure 10. Sensitivity to Zernike perturbations induced by different methods, both in the model and in the testbed. *Left.* Evaluated by averaging over $3 - 9\lambda/D$. *Right.* Evaluated by averaging over $3 - 4\lambda/D$, the most likely area to find planets.

3.3 Sensitivities

Understanding dynamic performance in the presence of error injection—and whether it meets expectations and requirements—requires understanding of coronagraph sensitivities to open-loop perturbations. We can derive these sensitivities by perturbed models, but if we want to believe these models, we also need to validate them against testbed data.

On the MCB testbed, perturbations for Z4-Z11 are introduced by low-order modulations on one of the DMs, using the same methodology to create shapes for correction in Section 2.2. (These perturbations are also sensitive to errors in knowledge of DM gain in the same way the corrections are; see [19] for a discussion and analysis.) Z4 can also come from source motion, in the same manner it was injected for MS9 dynamic testing. Z2/Z3 sensitivity can be measured in several ways: tilts on DM, FSM, or jitter mirror, or lateral motion of the focal plane mask (as pupil tilts because focal-plane translations). Sensitivities were calculated by fitting a second-order polynomial to the mean intensity across the region of interest. A similar approach is to fit a polynomial at each pixel, and then take the mean over the array of sensitivities; this approach was taken in [19] for analyzing SPC data, and produced consistent results.

Fig. 10 shows the measured and modeled sensitivities of the SPC on MCB, both over $3 - 9\lambda/D$ and over a subregion $3 - 4\lambda/D$. Normalized intensity was used here to avoid the bias induced by the contrast compensation.

4. NEXT STEPS

Upcoming tests on the MCB aim to increase flight-like fidelity of testbed operation. A particular focus will be operation at low SNR levels, which is consistent with the situation for coronagraphy on faint stars: we plan to demonstrate nulling to high-contrast dark holes with error injection and correction, while maintaining the LOWFS and imaging camera at flight-like SNR. We expect, as part of this, that the pairwise estimation will be replaced or augmented by a Kalman-filter-based estimator, which has shown superior performance relative to total exposure time[35].

Another area of upcoming work is better characterization of DM motion per volt per actuator. Correction of terms Z4 and above with the DM requires good open-loop accuracy of DM placement, and we will be doing a more comprehensive measurement of nm/V for each actuator on both DMs.

In the past, the MCB had a telescope simulator that had to be removed. Too large of a source diameter in λ/D created an undesirable amplitude distribution in subsequent pupils; this was fixed by reimaging the source pinhole at a different magnification, but this modification was unable to fit on the bench with the telescope simulator. Having acquired additional parts, we will be reinserting the simulator in combination with the magnification update, so the testbed fully introduces the fast front end of the telescope system. Finally, testing of the PISCES

IFS is ongoing on a separate testbed for operational efficiency, but eventually will be integrated into MCB as well; legs and a simulator plate are in place on MCB now to reserve its location.

To sum, we have demonstrated static and dynamic performance of the shaped pupil coronagraph architecture for WFIRST CGI in flight-like environments, and further testing will move the system demonstration to higher-fidelity representations of the future flight environment.

ACKNOWLEDGMENTS

References

[1] D.J. Des Marais, M.O. Harwit, K.W. Jucks, J.F. Kasting, D.N. Lin, J.I. Lunine, J. Schneider, S. Seager, W.A. Traub, and N.J. Woolf. Remote sensing of planetary properties and biosignatures on extrasolar terrestrial planets. *Astrobiology*, 2(2):153–181, 2002.

[2] O. Guyon, E. A. Pluzhnik, M. J. Kuchner, B. Collins, and S. T. Ridgway. Theoretical Limits on Extrasolar Terrestrial Planet Detection with Coronagraphs. *The Astrophysical Journal Supplement Series*, 167:81–99, November 2006.

[3] D. Spergel, N. Gehrels, C. Baltay, D. Bennett, J. Breckinridge, M. Donahue, A. Dressler, B. S. Gaudi, T. Greene, O. Guyon, C. Hirata, J. Kalirai, N. J. Kasdin, B. Macintosh, W. Moos, S. Perlmutter, M. Post-man, B. Rauscher, J. Rhodes, Y. Wang, D. Weinberg, D. Benford, M. Hudson, W.-S. Jeong, Y. Mellier, W. Traub, T. Yamada, P. Capak, J. Colbert, D. Masters, M. Penny, D. Savransky, D. Stern, N. Zim-merman, R. Barry, L. Bartusek, K. Carpenter, E. Cheng, D. Content, F. Dekens, R. Demers, K. Grady, C. Jackson, G. Kuan, J. Kruk, M. Melton, B. Nemati, B. Parvin, I. Poberezhskiy, C. Peddie, J. Ruffa, J. K. Wallace, A. Whipple, E. Wollack, and F. Zhao. Wide-Field InfrarRed Survey Telescope-Astrophysics Focused Telescope Assets WFIRST-AFTA 2015 Report. *ArXiv e-prints*, March 2015.

[4] W. A. Traub, M. Levine, S. Shaklan, J. Kasting, J. R. Angel, M. E. Brown, R. A. Brown, C. Burrows, M. Clampin, A. Dressler, H. C. Ferguson, H. B. Hammel, S. R. Heap, S. D. Horner, G. D. Illingworth, N. J. Kasdin, M. J. Kuchner, D. Lin, M. S. Marley, V. Meadows, C. Noecker, B. R. Oppenheimer, S. Seager, M. Shao, K. R. Stapelfeldt, and J. T. Trauger. TPF-C: status and recent progress. In *Society of Photo-Optical Instrumentation Engineers (SPIE) Conference Series*, volume 6268 of *Proceedings of the SPIE*, page 62680T, June 2006.

[5] J. Trauger, K. Stapelfeldt, W. Traub, J. Krist, D. Moody, D. Mawet, E. Serabyn, C. Henry, P. Brugarolas, J. Alexander, R. Gappinger, O. Dawson, V. Mireles, P. Park, L. Pueyo, S. Shaklan, O. Guyon, J. Kasdin, R. Vanderbei, D. Spergel, R. Belikov, G. Marcy, R. A. Brown, J. Schneider, B. Woodgate, R. Egerman, G. Matthews, J. Elias, Y. Conturie, P. Vallone, P. Voyer, R. Polidan, C. Lillie, C. Spittler, D. Lee, R. Hejal, A. Bronowicki, N. Saldivar, M. Ealey, and T. Price. ACCESS: a concept study for the direct imaging and spectroscopy of exoplanetary systems. In *Society of Photo-Optical Instrumentation Engineers (SPIE) Conference Series*, volume 7731 of *Society of Photo-Optical Instrumentation Engineers (SPIE) Conference Series*, July 2010.

[6] O. Guyon, G. Schneider, R. Belikov, and D. J. Tenerelli. The EXoplanetary Circumstellar Environments and Disk Explorer (EXCEDE). In *Space Telescopes and Instrumentation 2012: Optical, Infrared, and Millimeter Wave*, volume 8442 of *Proceedings of the SPIE*, page 84421S, September 2012.

[7] O. Guyon, J. R. P. Angel, R. Belikov, R. Egerman, D. Gavel, A. Giveon, T. Greene, K. Cahoy, B. Kern, M. Levine, S. Ridgway, S. Shaklan, D. Tenerelli, R. Vanderbei, and R. A. Woodruff. Detecting and char-acterizing exoplanets with a 1.4-m space telescope: the Pupil mapping Exoplanet Coronagraphic Observer (PECO). In *Society of Photo-Optical Instrumentation Engineers (SPIE) Conference Series*, volume 7440 of *Society of Photo-Optical Instrumentation Engineers (SPIE) Conference Series*, August 2009.

[8] K. R. Stapelfeldt, M. P. Brenner, K. R. Warfield, F. G. Dekens, R. Belikov, P. B. Brugarolas, G. Bryden, K. L. Cahoy, S. Chakrabarti, S. Dubovitsky, R. T. Effinger, B. Hirsch, A. Kissil, J. E. Krist, J. J. Lang, M. S. Marley, M. W. McElwain, V. S. Meadows, J. Nissen, J. M. Oseas, E. Serabyn, E. Sunada, J. T. Trauger, and S. C. Unwin. Exo-C: a probe-scale space mission to directly image and spectroscopically characterize exoplanetary systems using an internal coronagraph. In *Space Telescopes and Instrumentation 2014: Optical, Infrared, and Millimeter Wave*, volume 9143 of *Proceedings of the SPIE*, page 91432K, August 2014.

[9] O. Guyon, P. M. Hinz, E. Cady, R. Belikov, and F. Martinache. High Performance Lyot and PIAA Coronagraphy for Arbitrarily Shaped Telescope Apertures. *The Astrophysical Journal*, 780:171, January 2014.

[10] M. N'Diaye, R. Soummer, L. Pueyo, A. Carlotti, C. C. Stark, and M. D. Perrin. Apodized Pupil Lyot Coronagraphs for Arbitrary Apertures. V. Hybrid Shaped Pupil Designs for Imaging Earth-like planets with Future Space Observatories. *The Astrophysical Journal*, 818:163, February 2016.

[11] G. Ruane, J. Jewell, D. Mawet, L. Pueyo, and S. Shaklan. Apodized vortex coronagraph designs for segmented aperture telescopes. In *Advances in Optical and Mechanical Technologies for Telescopes and Instrumentation II*, volume 9912 of *Proceedings of the SPIE*, page 99122L, July 2016.

[12] M. R. Bolcar, K. Balasubramanian, J. Crooke, L. Feinberg, M. Quijada, B. J. Rauscher, D. Redding, N. Rioux, S. Shaklan, H. P. Stahl, C. M. Stahle, and H. Thronson. Technology gap assessment for a future large-aperture ultraviolet-optical-infrared space telescope. *Journal of Astronomical Telescopes, Instruments, and Systems*, 2(4):041209, October 2016.

[13] A. J. E. Riggs, N. Zimmerman, A. Carlotti, N. J. Kasdin, and R. Vanderbei. Shaped pupil design for future space telescopes. In *Society of Photo-Optical Instrumentation Engineers (SPIE) Conference Series*, volume 9143 of *Society of Photo-Optical Instrumentation Engineers (SPIE) Conference Series*, page 25, August 2014.

[14] J. Trauger, D. Moody, and B. Gordon. Complex apodized Lyot coronagraph for exoplanet imaging with partially obscured telescope apertures. In *Society of Photo-Optical Instrumentation Engineers (SPIE) Conference Series*, volume 8864 of *Society of Photo-Optical Instrumentation Engineers (SPIE) Conference Series*, page 12, September 2013.

[15] Ruslan Belikov, Amir Giveon, Brian Kern, Eric Cady, Michael Carr, Stuart Shaklan, Kunjithapatham Balasubramanian, Victor White, Pierre Echternach, Matt Dickie, John Trauger, Andreas Kuhnert, and N. Jeremy Kasdin. Demonstration of high contrast in 10 percent broadband light with the shaped pupil coronagraph. volume 6693. SPIE, 2007.

[16] A. J. E. Riggs, T. D. Groff, A. Carlotti, N. J. Kasdin, E. J. Cady, B. D. Kern, and A. Kuhnert. Demonstration of symmetric dark holes using two deformable mirrors at the high-contrast imaging testbed. In *Society of Photo-Optical Instrumentation Engineers (SPIE) Conference Series*, volume 8864 of *Society of Photo-Optical Instrumentation Engineers (SPIE) Conference Series*, page 0, September 2013.

[17] J. Trauger, D. Moody, B. Gordon, J. Krist, and D. Mawet. A hybrid Lyot coronagraph for the direct imaging and spectroscopy of exoplanet systems: recent results and prospects. In *Techniques and Instrumentation for Detection of Exoplanets V*, Proceedings of the SPIE, 2011.

[18] B.-J. Seo, E. Cady, B. Gordon, B. Kern, D. Marx, D. Moody, R. Muller, K. Patterson, I. Poberezhskiy, F. Shi, E. Sidick, J. Trauger, and D. Wilson. Hybrid Lyot coronagraph for WFIRST: high-contrast broadband testbed demonstration. In *Techniques and Instrumentation for Detection of Exoplanets VIII*, volume 10400 of *Proceedings of the SPIE*, pages 10400–15, August 2017.

[19] H. Zhou, B. Nemati, J. Krist, E. Cady, B. Kern, and I. Poberezhskiy. Wavefront Control Performance Modeling with WFIRST Shaped Pupil Coronagraph Testbed. In *Techniques and Instrumentation for Detection of Exoplanets VIII*, volume 10400 of *Proceedings of the SPIE*, pages 10400–5, August 2017.

[20] T. Groff, O. Guyon, C. Mejia Prada, E. Cady, M. Rizzo, P. Saxena, A. Mandell, Q. Gong, M. McElwain, and N. J. Kasdin. Wavefront control methods for high-contrast integral field spectroscopy. In *Techniques and Instrumentation for Detection of Exoplanets VIII*, volume 10400 of *Proceedings of the SPIE*, pages 10400–24, August 2017.

[21] E. Cady, C. M. Prada, X. An, K. Balasubramanian, R. Diaz, N. J. Kasdin, B. Kern, A. Kuhnert, B. Nemati, I. Poberezhskiy, A. J. Eldorado Riggs, R. Zimmer, and N. Zimmerman. Demonstration of high contrast with an obscured aperture with the WFIRST-AFTA shaped pupil coronagraph. *Journal of Astronomical Telescopes, Instruments, and Systems*, 2(1):011004, January 2016.

[22] B.-J. Seo, B. Gordon, B. Kern, A. Kuhnert, D. Moody, R. Muller, I. Poberezhskiy, J. Trauger, and D. Wilson. Hybrid Lyot coronagraph for wide-field infrared survey telescope-astrophysics focused telescope assets: occulter fabrication and high contrast narrowband testbed demonstration. *Journal of Astronomical Telescopes, Instruments, and Systems*, 2(1):011019, January 2016.

[23] F. Shi, K. Balasubramanian, R. Hein, R. Lam, D. Moore, J. Moore, K. Patterson, I. Poberezhskiy, J. Shields, E. Sidick, H. Tang, T. Truong, J. K. Wallace, X. Wang, and D. Wilson. Low-order wavefront sensing and control for WFIRST-AFTA coronagraph. *Journal of Astronomical Telescopes, Instruments, and Systems*, 2(1):011021, January 2016.

[24] A. Give'on, B. D. Kern, and S. Shaklan. Pair-wise, deformable mirror, image plane-based diversity electric field estimation for high contrast coronagraphy. In *Society of Photo-Optical Instrumentation Engineers (SPIE) Conference Series*, volume 8151 of *Society of Photo-Optical Instrumentation Engineers (SPIE) Conference Series*, September 2011.

[25] A. Give'on. A unified formalism for high contrast imaging correction algorithms. volume 7440, page 74400D. SPIE, 2009.

[26] D. Marx, B.-J. Seo, E. Sidick, B. Kern, B. Nemati, and I. Poberezhskiy. Electric field conjugation in the presence of model uncertainty. In *Techniques and Instrumentation for Detection of Exoplanets VIII*, volume 10400 of *Proceedings of the SPIE*, pages 10400–23, August 2017.

[27] E. E. Bloemhof and J. K. Wallace. Phase-contrast wavefront sensing for adaptive optics. In J. D. Gonglewski, M. T. Gruneisen, and M. K. Giles, editors, *Advanced Wavefront Control: Methods, Devices, and Applications II*, volume 5553 of *Proceedings of the SPIE*, pages 159–169, October 2004.

[28] O. Guyon. Limits of Adaptive Optics for High-Contrast Imaging. *The Astrophysical Journal*, 629:592–614, August 2005.

[29] X. Wang, J. K. Wallace, and F. Shi. Zernike wavefront sensor modeling development for LOWFS on WFIRST-AFTA. In *Techniques and Instrumentation for Detection of Exoplanets VII*, volume 9605 of *Proceedings of the SPIE*, page 960528, September 2015.

[30] K. Patterson, J. Shields, X. Wang, H. Tang, A. Azizi, P. Brugarolas, M. Mandic, and F. Shi. Control design for momentum-compensated fast steering mirror for WFIRST-AFTA coronagraph instrument. In *Techniques and Instrumentation for Detection of Exoplanets VII*, volume 9605 of *Proceedings of the SPIE*, page 96052C, September 2015.

[31] F. Shi, X. An, K. Balasubramanian, R. Bartos, E. Cady, B. Kern, r. Lam, D. Marx, C. Mejia Prada, D. Moody, R. Muller, K. Patterson, I. Poberezhskiy, A. J. E. Riggs, D. Ryan, B.-J. Seo, C. Shelton, J. Shields, E. Sidick, H. Tang, J. Trauger, T. Truong, V. White, D. Wilson, H. Zhou, and R. Zimmer. Testbed demonstration of low-order wavefront sensing and control for WFIRST coronagraph. In *Techniques and Instrumentation for Detection of Exoplanets VIII*, volume 10400 of *Proceedings of the SPIE*, pages 10400–13, August 2017.

[32] N. T. Zimmerman, A. J. Eldorado Riggs, N. Jeremy Kasdin, A. Carlotti, and R. J. Vanderbei. Shaped pupil Lyot coronagraphs: high-contrast solutions for restricted focal planes. *Journal of Astronomical Telescopes, Instruments, and Systems*, 2(1):011012, January 2016.

[33] K. Balasubramanian, D. Wilson, V. White, R. Muller, M. Dickie, K. Yee, R. Ruiz, S. Shaklan, E. Cady, B. Kern, R. Belikov, O. Guyon, and N. J. Kasdin. High contrast internal and external coronagraph masks produced by various techniques. In *Society of Photo-Optical Instrumentation Engineers (SPIE) Conference Series*, volume 8864 of *Society of Photo-Optical Instrumentation Engineers (SPIE) Conference Series*, page 1, September 2013.

[34] K. Balasubramanian, V. White, K. Yee, P. Echternach, R. Muller, M. Dickie, E. Cady, C. M. Prada, D. Ryan, I. Poberezhskiy, B. Kern, H. Zhou, J. Krist, B. Nemati, A. J. Eldorado Riggs, N. T. Zimmerman, and N. J. Kasdin. WFIRST-AFTA coronagraph shaped pupil masks: design, fabrication, and characterization. *Journal of Astronomical Telescopes, Instruments, and Systems*, 2(1):011005, January 2016.

[35] A. Eldorado Riggs, N. J. Kasdin, and T. D. Groff. Recursive Starlight and Bias Estimation for High-Contrast Imaging with an Extended Kalman Filter. *Journal of Astronomical Telescopes, Instruments, and Systems*, 2(1), January 2016.